USE OF EISCAT 3D FOR OBSERVATIONS OF SPACE DEBRIS

J. Vierinen[(1)], **J. Markkanen**[(2)], **H. Krag**[(3)], **J. Siminski**[(3)], **and A. Mancas**[(3)]

[(1)]*University of Tromsø, Hansine Hansens veg 18, 9019 Tromsø, Norway, Email: jvi019@uit.no*
[(2)]*EISCAT Scientific Association, Sodankylä, Finland*
[(3)]*ESA/ESOC Space Debris Office, Darmstadt, Germany*

ABSTRACT

We investigate the capabilities of the next generation ionospheric research radar EISCAT 3D (E3D) for observations of space objects. The radar is multi-static, and is therefore capable of observing instantaneous three-dimensional vector velocity and position by observing round-trip delay and Doppler shift between the transmitter and three receiver sites. The radar is to be located in Northern Scandinavia, which provides a high revisit-rate for high inclination objects. To model the performance of E3D for space object observations, we have included radar equation based analysis of object detectability as a function of range and size. To study the performance of the radar for orbital elements determination, we have used a linearized error covariance analysis for idealized Keplerian elements. The analysis includes range and range-rate errors due to signal-to-noise and ionospheric radio propagation. To estimate the fraction of total debris that can be observed with E3D, we have used the MASTER model [FGW+09]. E3D uses a relatively low VHF frequency (233 MHz), which experiences more radio wave propagation effects than more conventional higher frequency space surveillance radars. Our modeling shows that ionospheric ray-bending and group delay are severe enough that these effects need to be modeled in order to determine accurate orbital elements. As EISCAT 3D is an ionospheric research radar, there will be high quality ionospheric electron density measurements that can be utilized for radio propagation modeling. Our simulations indicate that the radar can be used for observations of orbital elements of objects down to 5 cm in diameter. It is therefore feasible that the radar could provide to be a useful source of accurate information of orbital elements of space debris.

Keywords: Radar, Space object tracking.

1. INTRODUCTION

Study of space debris is listed in the Science Case for EISCAT 3D [MAA+15] as one of the application areas of the planned next generation multi-static high-power large-aperture (HPLA) radar planned in Northern Fenno-Scandinavia. The primary mission for the radar is however ionospheric science, which means that it the driver for the radar design was not space object observations. In this study, we have set out to investigate in greater detail the utility of E3D for space object observations – both for beam-park observations, and for surveillance purposes. We will use the current projected design of E3D as basis of this study.

To model the performance of E3D for space debris observations, we have studied radar equation based detectability and performed an error analysis for range and range-rate observables [MLHV02]. Because the radar will be multi-static, it is capable of observing instantaneous three-dimensional vector velocities and positions by observing delay and Doppler shift between the transmitter and three or more receiver sites. We have included linearized error estimates for Keplerian orbital elements based on multi-static observations of targets. We have intentionally chosen not to use a more complicated orbit model, in order to get a simple and intuitive first order idea of orbit determination accuracy and repeat-rate of observations.

E3D uses a relatively low VHF frequency (233 MHz), which experiences more radio wave propagation effects than more conventional higher frequency surveillance radars. Our modeling shows that ionospheric ray-bending and group delay are severe enough that these effects need to be addressed if one were to utilize E3D for accurate orbital elements determination. Without ionospheric corrections, measurements performed using E3D are unusable for determining useful orbital elements. Because E3D is an ionospheric research radar, it can measure electron density profiles at the same time with every measurement of a space object, and this can be used to correct for propagation errors. In order to obtain a more realistic model of errors, we have estimated residual ionospheric propagation errors after ionospheric propagation corrections have been applied, and used these errors when estimating orbital elements determination performance.

2. EISCAT 3D

The EISCAT 3D radar (E3D) is a a multi-static HPLA radar, which is to be located in Northern Scandinavia. The radar uses phased array antennas for transmit and receive. The radar will initially have one transmit and receive site in Skibotn, Norway (69.340°N, 20.313°E). There will also be four receive-only sites: Karesuvanto (68.463°N,22.458°E), Bergfors (68.148°N, 19.769°E), Andoya Norway (69.251°N, 16.096°E) and Jokkmokk (66.60° N, 19.81° S). The technical description of the planned radar is described in detail in the technical note published by EISCAT [EIS14]. The planned locations are shown on a map in in Figure 1.

The plan is to build E3D in two stages. In the first stage, a transmitter and receiver will be located in Skibotn. Receivers will be located in Karesuvanto and Bergfors. In the next stage, two more receivers will be built: one in Andoya and one in Jokkmokk.

Currently planned parameters for E3D are listed in the Table 1. In this table, N_{beams} stands for the number of simultaneous beams that can be formed, T_{rec} stands for receiver noise temperature, and B_{tx} is transmit bandwidth. The transmit power P_{tx} is planned to be 10 MW.

The radar will have a center frequency of 233 MHz. Each antenna array will consist of 9919 inverted-v dipole antenna elements similar to the PAVE PAWS design [BPC+10], grouped under 91 antenna subgroups. The array will be a planar array placed horizontally with the on-axis direction pointing towards zenith. The antenna arrays have a full-width half maximum beam width of approximately 0.9°. The antennas are steerable to 60° off zenith, with gain falling off approximately according to projected geometric area $G(\alpha) = G_0 \cos(\alpha)$, where α is the zenith angle.

The Skibotn transmitter site will have interferometric outlier antennas, which are approximately 10 meters in diameter. The longest baseline will be approximately 1.5 km. The main purpose of the spaced antenna interferometer is to perform imaging of small-scale ionospheric structure in the E-region of the ionosphere during auroral energetic electron precipitation. The interferometry will also have uses for measurements of trajectories of micrometeoroids [KSN+12], and for planetary radar measurements of the Moon [Tho87]. These interferometric antennas may also have utility when estimating the angle of arrival of high signal-to-noise ratio space debris targets with high precision. It is also possible to divide the core antenna into subarrays for interferometry. Figure 7 shows an example of a mono-pulse type of an interferometer, achieved by dividing the core array into four quadrants.

The antenna will have an all-digital beamformer, with a direct sampling 105 MHz digitizer connected to two polarizations on each one of the 9919 antenna elements. A level one beamformer will reduce the bandwidth to 30 MHz and form up to 10 dual polarization beams on each one of the 91 element tiles. These first level wide angle

Site	Gain dBi	N_{beams}	TX	T_{rec} K	B_{tx} MHz
Skibotn	43	100	yes	150	≤ 5
Bergfors	43	100	no	150	
Karesuvanto	43	100	no	150	
Jokkmokk	43	100	no	150	
Karesuvanto	43	100	no	150	

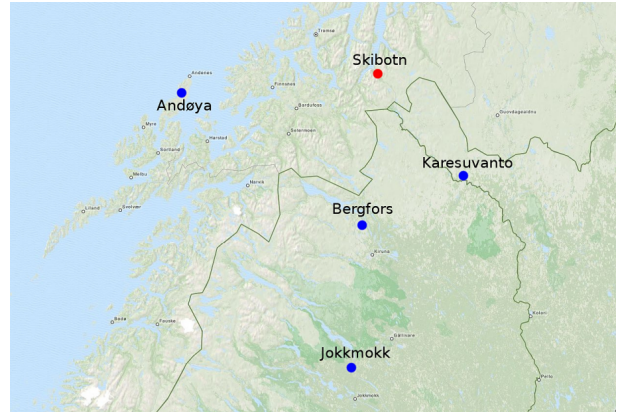*Table 1. The performance parameters for E3D.*

Figure 1. Planned E3D sites. The core site in Skibotn is colored with red. Receive sites are located in Karesuvanto, Bergfors, Andoya, and Jokkmokk are colored with blue.

beams are then used by the second level beamformer to form up to 100 dual polarization 30 MHz beams. On the core site, most of these beams will be utilized for interferometry. On the receive sites, these beams will be used to form beams that intersect the transmitter beam across all altitudes of interest. The number of beams is sufficient to simultaneously cover all common volumes with the transmit beam. An example of a transmit beam intersecting with 100 receive beams is shown in Figure 2.

The second level beamformer and the high level signal processing will be implemented using a general purpose high performance computing cluster. The e-infrastructure for E3D is still in somewhat formative stages, and it is not yet decided if the second level beamformed data will be transmitted over a fast internet connection to a central supercomputer for analysis, or if the supercomputer will reside at the location of the radar site. The most likely scenario is that the vast majority of computing will be performed on-site and accomplished by having extra computational resources for analyzing and reducing the radar data before sending it to a central archive. The latter scenario will allow low-latency analysis to be performed, allowing that radar to quickly adapt to changing conditions. It is feasible that the radar will be able to allocate beams in a sub-second timescale to follow transient targets, such as meteors, or space debris.
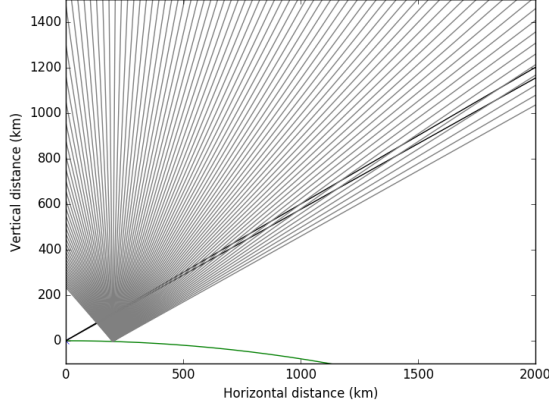
Figure 2. Conceptual diagram of a $1°$ transmit beam intersected by 100 receive beams from a bi-static receive array to cover common volumes across a wide range of altitudes. The Earth's surface is depicted with a green line.
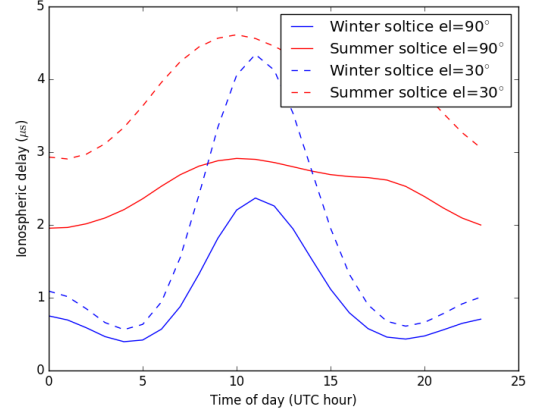
Figure 3. Ionospheric propagation delays at two representative times of year: 1) summer solstice, when electron density is at highest, and 2) winter solstice, when ionospheric electron densities are at minimum. The vertical pointing and lowest elevation that E3D is capable of are shown. The calculation takes into account ionospheric group delay, and ray-bending effects. The delay is excess delay to target compared to a ray propagating in vacuum.

3. RADIO PROPAGATION

The carrier frequency of E3D is $f = 233$ MHz. This is high enough that the magnetic field can be to first order ignored when estimating the range measurement errors that are caused by ionospheric radio propagation. However, the electron density cannot be ignored. Ionospheric plasma is a dielectric medium, with a dielectric constant [Bud88]

$$\epsilon = \left(1 - \frac{\omega_p^2}{\omega^2}\right)\epsilon_0. \quad (1)$$

The refractive index for a radio wave propagating in plasma is:

$$n = \sqrt{1 - \frac{f_p^2}{f^2}} \quad (2)$$

where $f_p \approx 8.98\sqrt{N_e}$ and f is the radio wave frequency and N_e is electron density (m^{-3}). The group velocity of a radio wave in this case is

$$v_g = c\sqrt{1 - \frac{f_p^2}{f^2}}. \quad (3)$$

Both of these assume no collisions or magnetic field. The approximations are valid for sufficiently high radio wave frequencies $f \gg f_p$. In the ionosphere, a typical maximum value for f_p is 10 MHz.

The two main radio propagation effects that are important to take into account when measuring accurate distance are: 1) ray-bending, and 2) ionospheric group delay. We have taken into account both of these effects in our modeling.

To investigate the effects of ionospheric dispersive radio wave propagation, we have implemented a ray-tracer.

This ray-tracer uses the IRI-model [BR08] to model the ionospheric electron density at any given geographic coordinate. The model includes both the effects of radio wave group velocity in the ionospheric plasma, and the ray-bending that occurs due to gradients in electron density.

Ray-bending in a medium with variable electron density can be to first order estimated using Snell's law instantaneously at any given point in space:

$$\frac{\sin\theta_1}{\sin\theta_2} = \frac{n_2}{n_1}, \quad (4)$$

where θ_1 is the angle of the radio wave $\boldsymbol{k}$-vector going through an interface, and θ_2 is the angle of the radio wave going out of the interface. The normal vector of the "interface" in this case is the gradient of the electron density ∇N_e. For each step of the iteration, the $\boldsymbol{k}$-vector is modified due to ray-bending using:

$$\mathbf{k}_{i+1} = \left(\frac{n_1}{n_2}\right)\mathbf{k}_i + \left(\frac{n_1}{n_2}\cos\theta_1 - \cos\theta_2\right)\nabla N_e \quad (5)$$

Here n_1 and n_2 is the refractive index of the medium at on the two sides of the boundary.

The ray-tracer numerically evaluates the propagation of the radio wave using the following Riemann sum approximation:

$$\mathbf{p}_N = \sum_{m=0}^{N-1}\frac{\mathbf{k}_m}{\|\mathbf{k}_m\|}\tau v_m \quad (6)$$

to obtain the location p_m at time $m\tau$. Here v_m is in-situ group velocity of the wave packet. The time step τ is
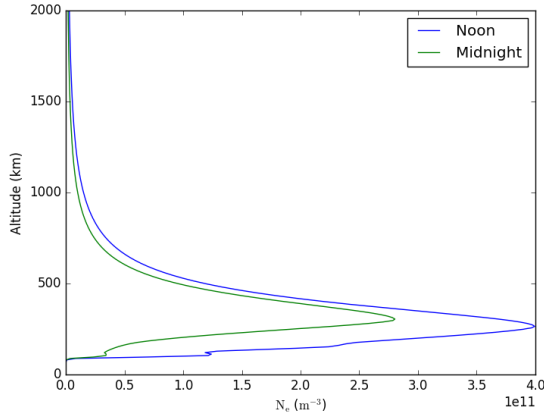
Figure 4. IRI model based electron density profile at summer solstice during noon and midnight.

chosen to be small enough that the solution converges. As we use the group velocity of the radio wave, the ray-tracer also models the total group delay, in addition to ray-bending.

3.1. Simulations

The ionospheric electron density is known to vary considerably throughout the year. During the winter, the high-latitude hemisphere is mostly not sunlit, causing the photoionization to be non-existent or reduced, due to low solar elevation angle. Due to this factor, the electron densities are low during the winter, and lowest during winter midnight. Conversely, during the summer, the high latitude hemisphere is constantly sunlit and the electron densities are higher.

For our simulations, we have selected midnight winter solstice and noon summer solstice as two extreme ionospheric conditions. During the winter, one expects the ionospheric propagation effects to be smallest, and during the summer the effects are maximized. The IRI model base ionospheric electron density profile above Skibotn is shown in Figure 4 for summer solstice noon and midnight.

The angle at which the radio wave is launched effects the distance that the radio wave propagates through the ionosphere. At lowest elevation angles, ionospheric radio propagation effects are largest, maximizing ray-bending and refractive delays. At zenith launch angle, the gradients are the smallest. But even in this case, there are horizontal gradients, which are mostly due to variable solar zenith angle as a function of latitude and longitude. These gradients are largest during sunrise and sunset periods. These gradients are represented by the ionospheric model.

Figure 3 shows excess delay to the signal due to iono-

spheric group velocity and ray-bending at four representative cases: 1) summer solstice, zenith pointing direction, 2) summer solstice low elevation, 3) winter solstice zenith pointing, and 4) winter solstice low elevation pointing direction. The delay is one-way. In the case of radar measurements, this needs to be doubled, as the radio wave must also propagate back through the same ionosphere. In all cases, the ionospheric one-way delay is less then 5 μs. This will result in a total additional round-trip range of 1.5 km! If not corrected for, this delay will already cause an unacceptably large error in a range measurement.

Our simulations do not take into account auroral precipitation, which can cause very large horizontal and vertical gradients in electron densities. Such conditions are often observed at high latitudes. It is probable that during auroral conditions, it will be more difficult to correct for ionospheric radio propagation effects. However, the radar measurements can be used as a diagnostic to identify the presence of more problematic radio propagation conditions.

3.2. Ionospheric error model

Based on ray-tracing simulations, it is imperative that ionospheric radio propagation modeling is used to correct space object observations. This can potentially be done, because E3D is an ionospheric radar that will be able to measure high quality ionospheric electron density profiles using a technique called incoherent scatter radar [Eva69]. Measurements of ionospheric electron density will still have errors [Val88], and these errors also will propagate into into the ionospheric corrections. We will call this post ionospheric correction error the "ionospheric propagation error".

To determine, to first order, what the magnitude of errors are after ionospheric propagation corrections have been applied, we have first modeled radio propagation using ray-tracing with a perfectly known ionosphere. This serves as the ground truth. We have then simulated a E3D electron density profile measurements, with simulated measurement errors. The same ray-tracing is then performed on the ionospheric measurement that contains errors. Due to the errors, the ray-tracing result differs from the ground truth, and any residual error can be assumed to be due to measurement errors in the electron density. The residual round-trip propagation delay error in this case is approximately $\tau_{\mathrm{res}} \approx 2|(\boldsymbol{p'} - \boldsymbol{p}) \cdot \boldsymbol{k}^0|/c$, where τ_{res} is error in round-trip delay, $\boldsymbol{p'}$ is the true location of the target, $\boldsymbol{p}$ is the position of the target obtained using a radar measurement based electron density. Here $\boldsymbol{k}^0$ is a unit vector indicating the propagation direction of the ray near the target. This is conceptually shown in Figure 5.

The post radio propagation correction errors are studied using Monte-Carlo sampling. We perform multiple radio propagation corrections with different random electron density errors. The mean value of the error is then
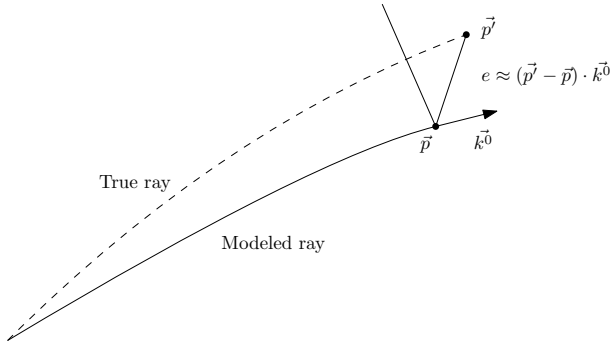
Figure 5. Determination of residual radio propagation errors. The difference between true propagation delay and the estimated propagation delay is calculated by estimating the residual distance e needed to meet the target.
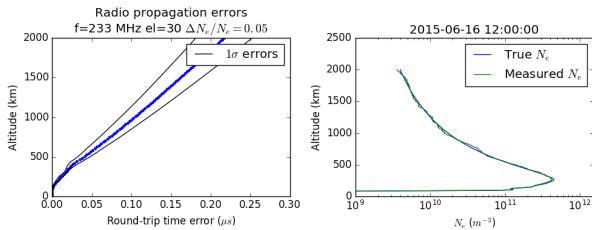

Figure 6. Worst-case residual errors due to ionospheric radio propagation, after applying corrections based on measured electron density.

calculated as a function of altitude. The results for the worst case scenario, summer solstice noon at low elevation pointing, are shown in Figure 6. In this case, the residual delay error due to ionospheric propagation is 0.2 μs at 2000 km. The main source of error above this altitude is due ray-bending. Any residual error in determining the amount of ray-bending increases the delay errors linearly as a function of range after the ray has passed the ionosphere. For further evaluations of orbital elements determination, we have chosen the worst case ionospheric errors. Based on Figure 6, we can model this with

$$e = 0.1(A/1000) \ \mu s, \qquad (7)$$

where e is delay error standard deviation in microseconds, and A is altitude in km.

4. RADAR PERFORMANCE MODEL

In order to study the performance of E3D for tracking orbital debris, we have created a software tool, which allows evaluating the performance of arbitrary multi-static radar configurations. The tool has the following features:

1. minimum detectable object size in the field of view of the radar network,

2. statistics of object measurement revisit rates, observation arcs, and orbital elements determination error; and

3. simulation of object detections in a beam-park observation.

The first functionality can be used to determine what fraction of all objects can be observed with a radar. The second feature determines how well a multi-static radar can determine orbital elements using all possible measurements of an object over some period of time. The beam-park simulation provides an estimate of the radar sensor response to unknown objects that are detected by a chance encounter. This allows us to estimate the rate of discovery of objects when the radar is operated in ionospheric research mode.

As a model of the population of objects in orbit, we use a catalog of objects specified with Keplerian orbits and diameter. We have used the MASTER 2009 model [FGW⁺09] as a model of objects in space. The population model is used to estimate what fraction of objects can be detected, and how well typical orbits of targets can be estimated.

The tool specifies a radar with the following parameters: transmit antenna gain G_{TX}, receive antenna gain G_{RX}, transmit peak power P_{TX}, transmit pulse length, inter-pulse period length, coherent integration time τ_{int}, system noise T, coordinates of transmit and receive antennas, and an elevation threshold. We assume that ionospheric radio propagation corrections can be made, as described in the previous section, and we use the range estimation errors after radio propagation corrections have been applied.

4.1. Radar observing mode

The radar transmit parameters used for these simulations assume a transmit pulse length of 2 ms, an inter-pulse period of 20 ms, coherent integration of 10 pulses, which results in 0.02 s of coherent integration. We assume a pseudorandom phase coded transmit pulse with a bandwidth of 1 MHz. This type of a radar mode is close to an optimal for observations of space objects, and is similar to the LEO mode that is used with existing EISCAT radars for observations of space objects. This mode is also fairly similar to a standard ionospheric survey mode, which E3D will use for its primary science mission.

4.2. Energy to noise

The Generalized Matched Function (GMF) has been shown to be a maximum likelihood estimate for target radial trajectory (range, range-rate, acceleration) [MLHV02]. The algorithm in use at EISCAT uses a variant called Fast Matched Function (FMF), which comes

close to the performance of GMF. The detection probability of an object depends on the ratio of time integrated power (energy) and noise. Typically, an ENR > 25 has been used as a detection threshold, but it is possible that with more sophisticated methods, this could be improved [Vie12].

Energy to noise ratio (ENR) is defined as:

$$\text{ENR} = \frac{P_{tx}G_{\text{tx}}G_{\text{rx}}\lambda^2\sigma\tau_{\text{int}}}{(4\pi)^3 R^4 kT} \qquad (8)$$

Here P_{tx} is transmit power, G is antenna gain, λ is wavelength, σ is radar cross-section τ_{int} is coherent integration time, R is range, k is the Boltzmann constant, and T is receiver noise temperature.

When determining if a target can be observed, we evaluate ENR for a target. Following [MLHV02], we assume that targets are perfectly conducting spheres when calculating radar cross-section. The scattering is assumed to be Rayleigh scattering when the diameter is smaller than the wavelength, and optical scattering when the object is wavelength is wavelength scale or larger. The radar cross-section equation is defined as:

$$\sigma = \begin{cases} \frac{9\pi^5}{4\lambda^4}d^6, & \text{when } d < \lambda/(\pi\sqrt{3}), \\ \frac{1}{4}\pi d^2 & \text{when } d > \lambda/(\pi\sqrt{3}), \end{cases} \qquad (9)$$

where d is the diameter of the object.

4.3. Antenna model

For the antenna, we assume a fully filled planar array with zenith on-axis. The antenna gain pattern is approximated using the Airy function. We include a full beam pattern in order to also account for cases where the target passes through the sidelobes of the antenna beam, which also often results in a detection of a target – this is especially important when modeling beam park observations or detections of new objects by chance encounter. We also take into account the broadening of the beam when the planar phased array antenna is pointed off axis.

4.4. Range and Doppler error model

In this study, we have considered only range and range-rate errors. We have not included a treatment for higher order radial trajectory parameters, such as acceleration. We assume that the radiated waveform is a random binary phase coded pulse with length τ_p and transmit bandwidth B_{TX}. Commonly used baud lengths for ionospheric research are in the range $1\ \mu s$ to 2 ms, which result in bandwidths of 500 Hz to 1 MHz. E3D can utilize up to 5 MHz of transmit bandwidth.

The measurement equation for a sampled point-target echo is approximated as:

$$m_t = \exp(i\omega\tau_s t)\text{env}_{t-R} + \xi_t = f(\omega, R, t) + \xi_t, \quad (10)$$

where $m_t \in \mathbb{C}$ is the measured signal, ω is the Doppler shift (rad/s), env_t is the transmitted waveform, τ_s is the sample duration, R is range in two-way light travel time in samples. The error $\xi_t \sim \mathcal{N}(0, \text{SNR}^{-1})$ is assumed to be proper complex normal random noise, with the signal-to-noise ratio SNR determined by the radar equation.

The measurement equation is discretized to a sufficient resolution. The transmit envelope is filtered using a Hamming window to present bandwidth B_{TX}. The non-linear function is linearized by numerical differentiation, so that the measurement equation is in the following form:

$$\boldsymbol{m} = \boldsymbol{J}\boldsymbol{x} + f(\boldsymbol{x_0}) + \boldsymbol{\xi}, \qquad (11)$$

here $\boldsymbol{x} = [R, \omega]^T$ is a vector containing the unknown values for range and Doppler, and $\boldsymbol{J}$ is a Jacobian containing the partial derivatives of the theory $J_{ij} = \frac{\partial f_i}{\partial x_j}$. The error vector $\boldsymbol{\xi}$ is distributed as $\mathcal{N}(0, \boldsymbol{\Sigma})$, where $\boldsymbol{\Sigma} = \text{diag}(\text{SNR}^{-1} \cdots \text{SNR}^{-1})$ and SNR is the signal to noise ratio of the target at simulation bandwidth.

The linearized error covariance is obtained with:

$$\boldsymbol{\Sigma_p} = (\boldsymbol{J}^H\boldsymbol{\Sigma}^{-1}\boldsymbol{J})^{-1}. \qquad (12)$$

We also only used the diagonal of the covariance matrix in our error model, $\text{diag}(\boldsymbol{\Sigma_p}) = [\sigma_R^2, \sigma_\omega^2]$, ignoring the correlation between the two unknown parameters, which is assumed to be low.

The modeled range and range-rate errors that are used as input for orbit determination error calculations also include ionospheric propagation errors, which we assume to be additive:

$$\boldsymbol{\Sigma_e} = \begin{bmatrix} \sigma_R^2 + \sigma_I^2 & 0 \\ 0 & \sigma_\omega^2 \end{bmatrix}, \qquad (13)$$

here σ_I^2 is the variance of ionospheric errors (Section 3.2).

4.5. Interferometric angle of arrival

The E3D radar is an all-digital phased array. This allows dividing the antenna on receive e.g., into four quadrants, to simulate a mono-pulse feed. We will use this as a baseline interferometer for estimating angle of arrival errors. This configuration is shown in Figure 7. In practice, more robust interferometry will be achieved by dividing the antenna into a larger number of subsections when determining angle of arrival.

Errors are again estimated using linearized error treatment. We assume that each antenna of the interferometer measures an angle of arrival dependent phase. Around the true peak value, we can assume linear behaviour:

$$\begin{bmatrix} z_0 \\ z_1 \\ z_2 \\ z_3 \end{bmatrix} = \begin{bmatrix} \frac{\partial e^{i\phi_0(\alpha,\beta)}}{\partial\alpha} & \frac{\partial e^{i\phi_0(\alpha,\beta)}}{\partial\beta} \\ \frac{\partial e^{i\phi_1(\alpha,\beta)}}{\partial\alpha} & \frac{\partial e^{i\phi_1(\alpha,\beta)}}{\partial\beta} \\ \frac{\partial e^{i\phi_2(\alpha,\beta)}}{\partial\alpha} & \frac{\partial e^{i\phi_2(\alpha,\beta)}}{\partial\beta} \\ \frac{\partial e^{i\phi_3(\alpha,\beta)}}{\partial\alpha} & \frac{\partial e^{i\phi_3(\alpha,\beta)}}{\partial\beta} \end{bmatrix} \begin{bmatrix} \alpha \\ \beta \end{bmatrix} + f(\hat{\alpha}, \hat{\beta}) + \boldsymbol{\xi}$$

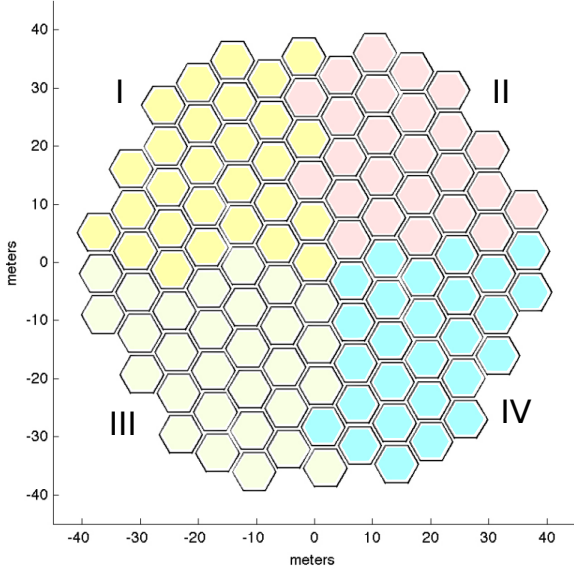$$= \boldsymbol{J}\boldsymbol{x} + f(\hat{\alpha}, \hat{\beta}) + \boldsymbol{\xi}$$

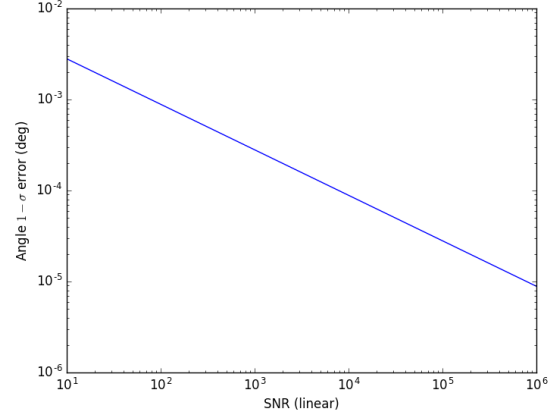Figure 7. Example interferometer that implements a simple four quadrant mono-pulse feed.

Figure 8. Sweep of linearized angle of arrival error as a function of ENR (post coherent integration) when dividing antenna into four quadrants.

Here $\phi_i(\alpha, \beta)$ is a function that translates antenna position to phase of the arriving signal and $\hat{\alpha}$ and $\hat{\beta}$ are true angles of arrival. The obtain linearized error covariance for parameters α and β for different signal-to-noise ratios ($\boldsymbol{\Sigma} = \mathrm{diag}(\mathrm{ENR}^{-1}, \cdots, \mathrm{ENR}^{-1})$), we evaluate the linearized a posteriori covariance matrix:

$$\boldsymbol{\Sigma_p} = (\boldsymbol{J}^H \boldsymbol{\Sigma}^{-1} \boldsymbol{J})^{-1}. \qquad (14)$$

Linearized error for angle of arrival standard deviation as a function of post coherent integration ENR is shown in Figure 8 for the interferometer shown in Figure 7. The figure only shows the value of one angle, because both angles have approximately the same error standard deviation.

4.6. Orbit determination error

Space debris objects are assumed to be in idealized Keplerian orbits, which are specified using six parameters: $\boldsymbol{x} = [e, a, i, \Omega, \omega, M_0]^T$, where e is eccentricity, a is semimajor axis, i is inclination, Ω is longitude of the ascending node, ω is argument of periapsis, and M_0 is the true anomaly. Orbital elements are also associated with an epoch, which fixes the position of the object at time t_0.

To estimate orbit determination errors for a set of measured parameters, we also have also used linearized error estimates. The non-linear Keplerian orbit model provides a relationship between the radar measurements of range $m_{R,t}$ and Doppler shift $m_{\nu,t}$ and the six elements $\boldsymbol{x}$.

$$\begin{aligned} m_{R,t} &= f_R(\boldsymbol{x}, t) + \xi_{R,t} \\ m_{\nu,t} &= f_\nu(\boldsymbol{x}, t) + \xi_{\nu,t} \end{aligned} \qquad (15)$$

The above equations are linearized and expressed in stacked matrix form (containing both range and Doppler observations):

$$\boldsymbol{m} = \boldsymbol{J}\boldsymbol{x} + f(\hat{\boldsymbol{x}}) + \boldsymbol{\xi}, \qquad (16)$$

here $\hat{\boldsymbol{x}}$ are the true orbital elements, $\boldsymbol{\xi}$ contains range and Doppler measurement errors, and $\boldsymbol{J}$ is the Jacobian. The covariance matrix for the six Keplerian elements is then:

$$\boldsymbol{\Sigma_p} = (\boldsymbol{J}^T \boldsymbol{\Sigma}^{-1} \boldsymbol{J})^{-1}. \qquad (17)$$

Here Σ is a diagonal error covariance matrix containing range and Doppler measurement errors (equation 13).

5. RESULTS

Minimum detectable target sizes at various altitudes in the geographic area around the radar is are shown in Figure 11. This plot only assumes stage 1 build-up with three receiver stations and one transmit site. Target is assumed to be detectable with an SNR of 10. At lower altitudes, the elevation cutoff limits the observation volume. Also, at lower elevation, the increased range and reduction in antenna gain lower the sensitivity.

Figure 10 shows noise equivalent object diameters at optimum detection geometry vertically above the Skibotn, with transmit and receive occurring there. The detection sensitivity is compared with several other radars: EISCAT UHF and the Arecibo 430 MHz radar. We also assume a hypothetical smaller tracking radar (TRA) with transmit power of 300 kW, a gain of 31 dB, and a wavelength of 20 cm. We assume the same coherent integration length for all radars. The sensitivity of E3D is not as good as the sensitivity of EISCAT UHF, mainly due to the significantly lower operating frequency.
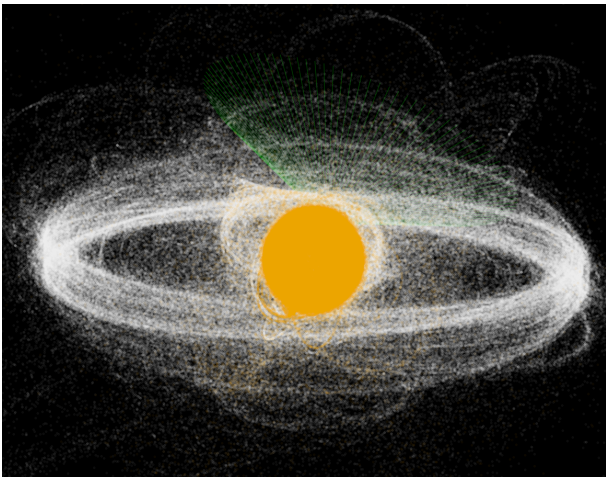
Figure 9. E3D field of view with respect to the orbital debris complex. Objects detectable with E3D are colored with orange. E3D is mainly sensitive to objects in low-Earth orbit that have a high enough inclination. However, high inclination orbits are the most common orbits for LEO debris, and have a high revisit rate at polar latitudes. The field of view of the E3D radar is shown with green lines.
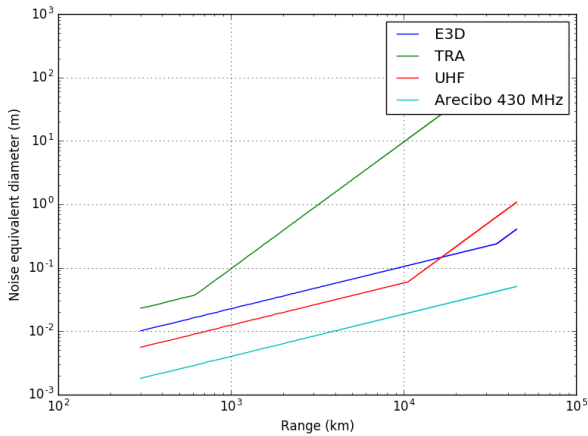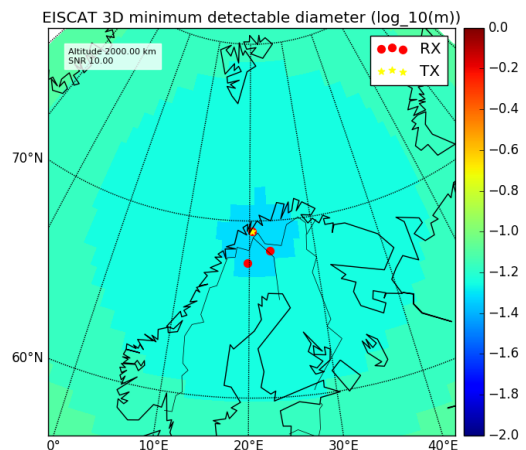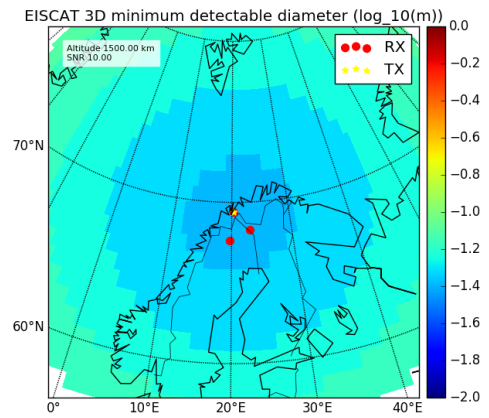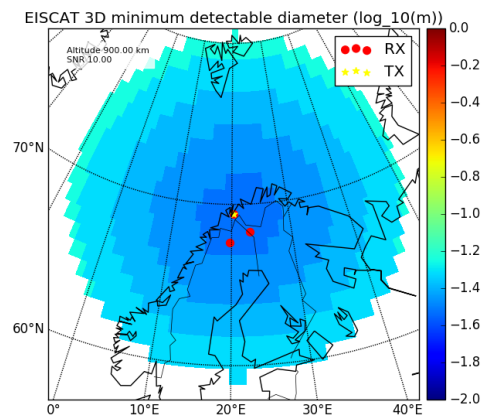

Figure 10. Receiver noise equivalenth diameter as a function of range for E3D. For comparison, the EISCAT UHF, the Arecibo 430 MHz radar, and a smaller L-band tracking radar (TRA) performance is shown. For each radar, we assume the same coherent integration length.
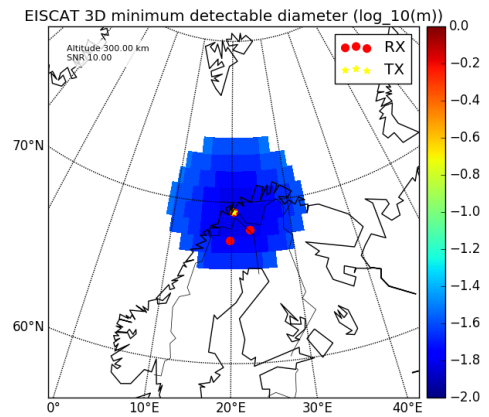
5.1. Detectable objects

To determine what objects E3D can observe, we went through the whole MASTER 2009 catalog of objects larger than 1 cm and evaluated positions of each object over 24 hours. We then selected the most favorable observing conditions for each objects and determined ENR. All objects with ENR > 1 where selected. We also determined if this detection was observable with at least three receiver stations. An overview rendering of the MASTER catalog objects is shown in Figure 9. In this figure, the E3D field of view is shown using green lines. Each object detectable with E3D is colored with orange, and each object not detectable with E3D is colored with grey.

Histograms of all objects vs. all detectable objects is shown in Figure 12. Histograms with respect to object diameter, inclination, minimum altitude, and ENR are shown. The objects below 3 cm start falling below the detection threshold. Also, objects with inclinations below 60° are in general not detectable, due to the high latitude location of the radar. If an object is detectable, it is in most cases detectable with at least three receiving stations. This means that nearly every measurement is a three-dimensional observation of target position and velocity. Corresponding cumulative sums are shown in Figure 13. At most around 10^5 objects can be observed using E3D, but most likely this number will be lower, as we selected receiver noise equivalent diameter as a threshold. There will also probably not be enough radar observing time observe this many objects in a routine manner to maintain a catalog of orbital elements.

5.2. Chance discovery

In order to estimate how many objects are observed by chance encounter by E3D, we evaluated a 24 hour beam-park observation. This will give an indication of how many untracked objects pass the beam when normal ionospheric observations are being performed. For this simulation we used a threshold of ENR = 100 as detection limit. A beam-park mode is very similar in nature to an ionospheric measurement that will be performed with E3D, and thus, new objects will to first order be discovered in a similar manner as a beam-park observation detects objects. If a more sophisticated scanning mode is implemented, the detection rate will be higher.

Figure 14 shows a comparison of beam-park detections as a function of target parameters between EISCAT UHF and E3D. Both radars see about the same number of objects per day, but E3D is not as sensitive to smaller objects due to the longer wavelength. The similar rate of objects is explained because of the wider beam opening angle of E3D. The total number of objects detected by chance using E3D system is around 2000, which is a significant fraction of the total number of objects that the radar could observe (about 2%).

5.3. Orbital Elements Determination

To simulate the orbital elements determination performance, we assume that the target can be picked up and followed. This is done either by knowing a prior what the approximate orbit is, or by determining it on first detection. All possible measurements over the course of a 24 hour period are considered for orbit determination. We assume that variability in e.g., atmospheric drag does not significantly effect the orbit over such a short period of time. Measurements are spaced 24 seconds apart from one another, to simulate a scenario where routine ionospheric observations are not affected by interleaved tracking measurements.

The range and range-rate measurements are used for orbit determination. Errors are estimated using the linearized error treatment for Keplerian orbits described in Section 4.6. Measurement errors take into account ionospheric errors and SNR based considerations for range. For range-rate, we just use the SNR based linearized errors, as we did not model ionospheric errors for the Doppler shift observable. Once an error covariance for the Keplerian parameters is formed, we sample the three dimensional position of the object in along-track, vertical, and horizontal directions by perturbing the Keplerian parameters with noise that has the error covariance structure. The samples are then used to calculate error ellipses.

We randomly sampled the MASTER 2009 catalog and performed an orbital elements error analysis. Figure 15 shows a characteristic plot of a simulated tracking measurement, with corresponding along-track, vertical, and cross-track errors. Typically, if the object can be measured at all, the errors in the determined orbital position are relatively small (< 10 m). LEO objects are typically well measured, due to high revisit rate. In many cases, it is also possible to determine orbital elements of Molniya orbits of larger objects. Smaller objects become more difficult to measure, because they can only be measured only overhead, not from horizon-to-horizon, as the received power falls fast as a function of range ($1/R^4$).

For all the objects we sampled and that could be used for orbital elements determination, we compiled statistics. Figure 16 shows a histogram of the number of tracklets that can be obtained per day for the sampled objects. A tracklet is defined as one horizon-to-horizon overflight of the object. Figure 17 shows the same as a scatterplot as a function of minimum altitude, eccentricity, inclination, and diameter.

CONCLUSIONS

The main conclusion is that E3D can be used for space object observations. The multi-static geometry is very powerful for measuring object trajectories, allowing for an instantaneous three dimensional position and velocity estimate. The high latitude location offers a high
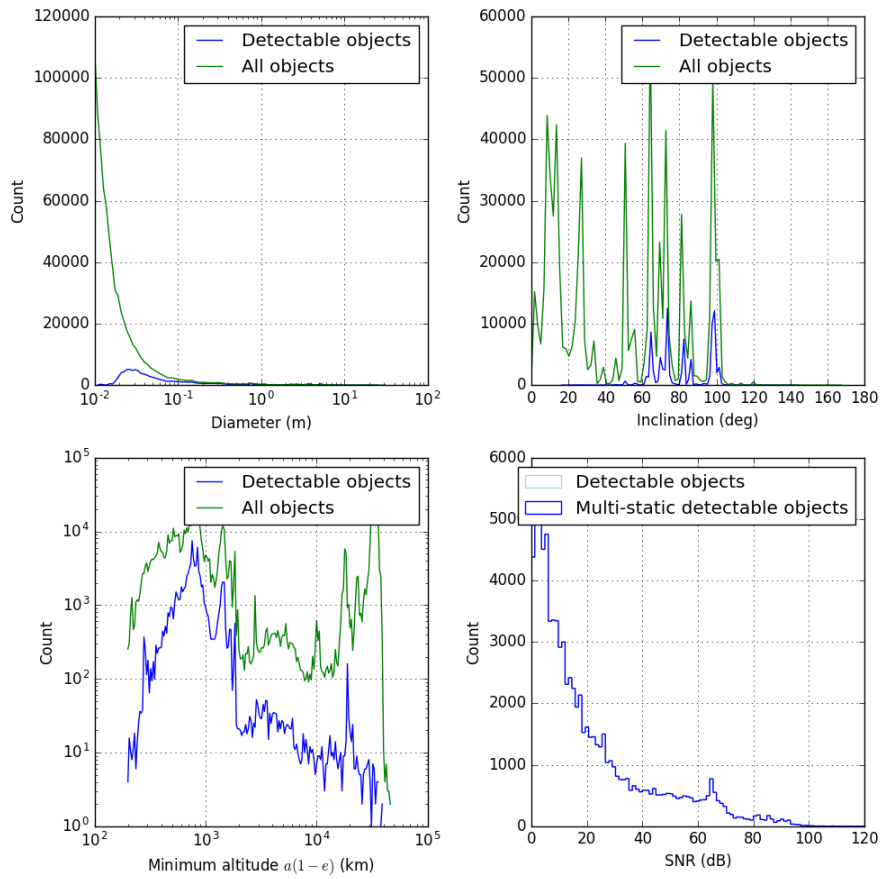
Figure 12. Histograms of all observable objects in the MASTER model. Low inclination objects cannot be observed due to high latitude location. Because of the long wavelength, objects below ≈ 3 cm fall below the observing threshold.
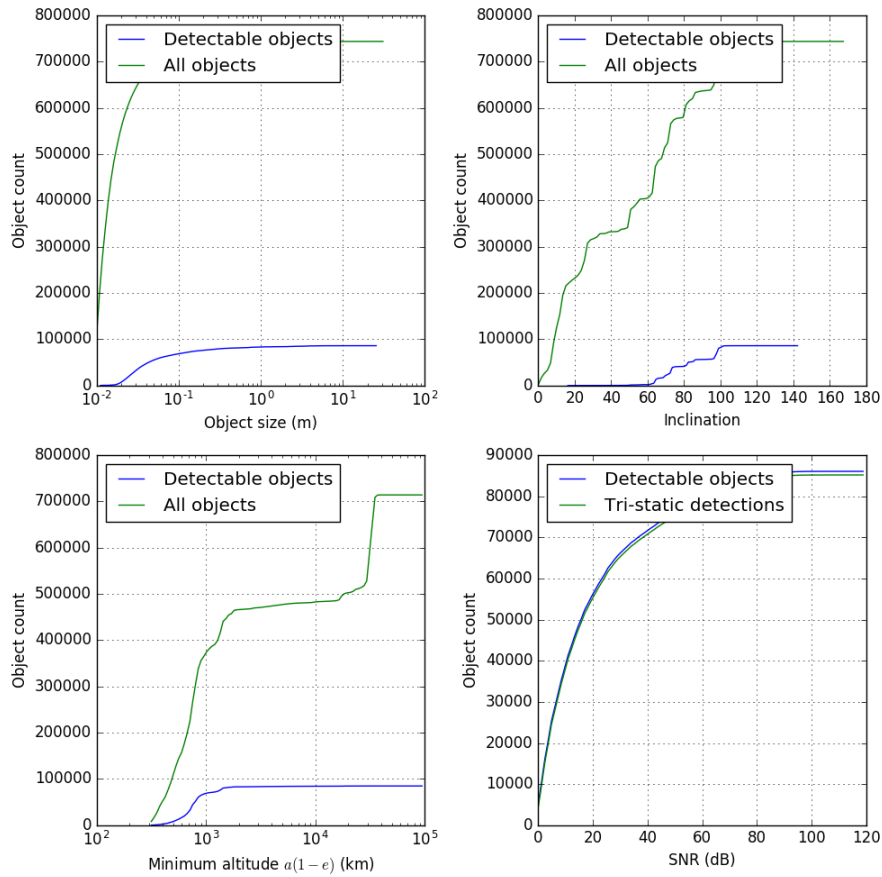
Figure 13. Cumulative sum of all observable objects in the MASTER model. Nearly 90000 objects out of 750000 can potentially be observed.
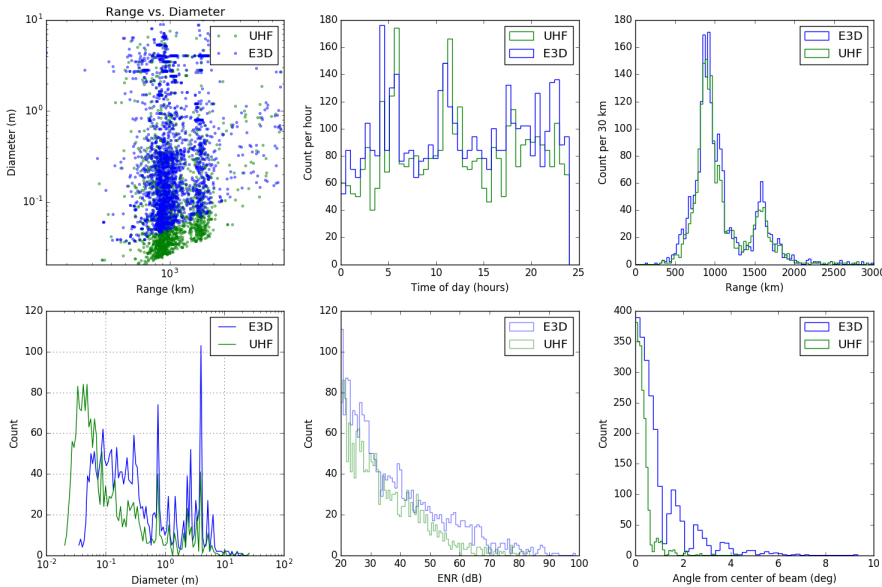

Figure 14. Beam-park comparison between EISCAT UHF and E3D. E3D is not as sensitive as the 930 MHz EISCAT UHF system for smaller objects that fall in the Rayleigh scattering regime, but it has a comparable detection rate, due to the wider beam.
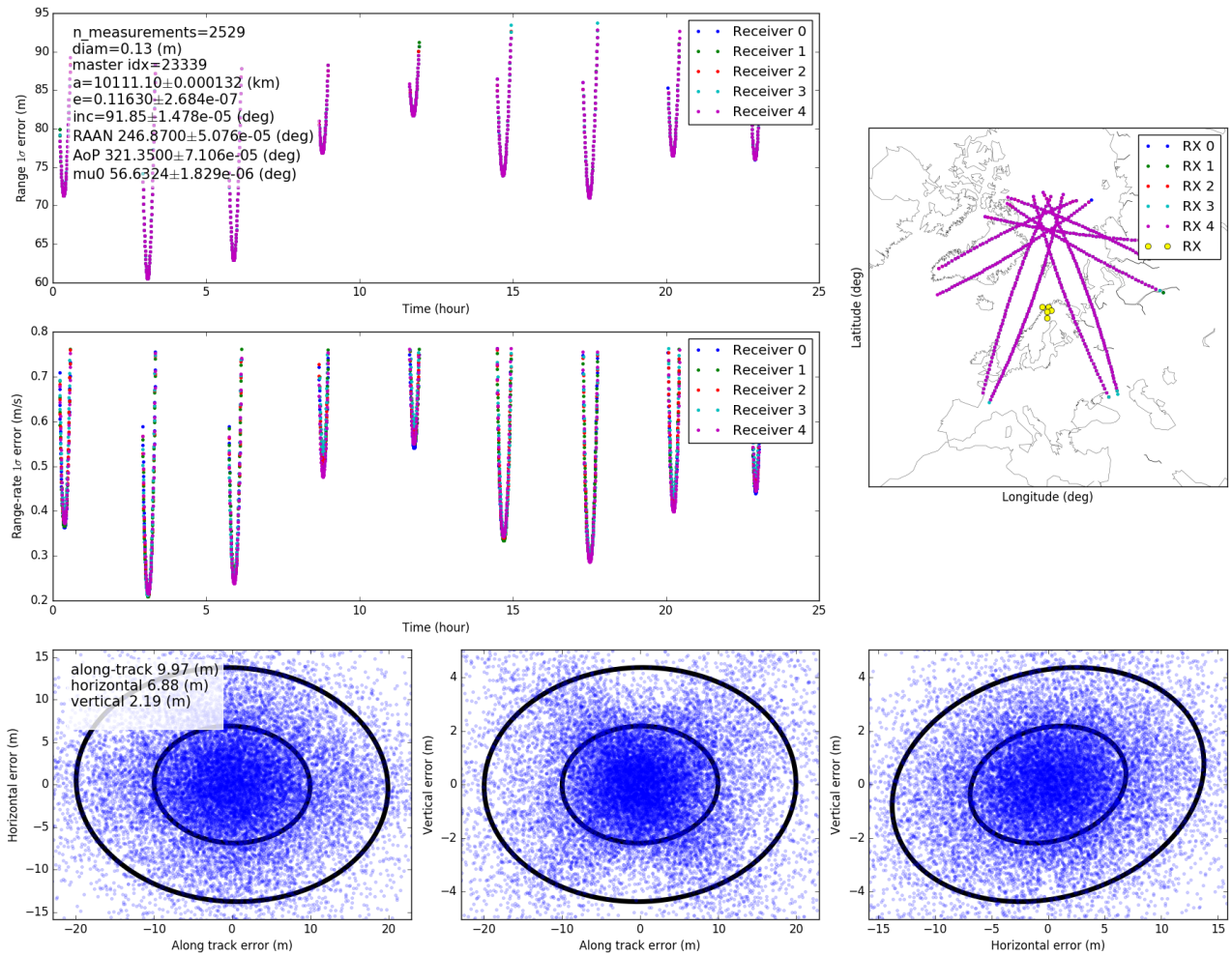
Figure 15. Orbital elements determination for a 13 cm object in polar orbit using all observations that are possible during a 24 hour time period. Top left: range errors during measurements, Middle left: Range-rate errors during measurements, Bottom panels: along-track, cross-track, and vertical errors in object position after orbital elements determination. Locations of the radar receivers and the ground footpoint of the space object during measurements are shown in the map on the top right.

Figure 16. Number of overflights per day histogram.

Figure 17. Number of overflights per day as a function of target parameters.

revisit rate for high inclination objects, which is useful as a large fraction of objects in LEO are in this orbital regime. While the E3D radar uses a frequency suboptimal for smaller objects, it can observe targets down to 3 cm objects in beampark mode, and useful tracking observations can probably be made with objects down to 5 cm in diameter.

In order for the radar to be useful for orbital elements determination, radio propagation effects need to be corrected for. As E3D is an ionospheric radar, the ionospheric plasma-parameters, including volumetric electron density, are always measured. This allows for accurate input to an ionospheric correction algorithm. Further validation is needed to ensure that ionospheric corrections can be made accurately, and to quantify the adverse effects of often present ionospheric irregularities for the accuracy of such corrections.

The strengths of E3D for space debris work include:

- capability to observe orbital elements,
- high latitude location, which provides high revisit rates for objects,
- fast beam steering capability,
- interferometric angle of arrival measurement,
- multi-static observation geometry,
- ionospheric electron density measurement,
- wide beam opening angle that enables efficient discovery of new objects, and
- a highly versatile high performance computing signal processing backend.

The drawbacks of E3D for space debris work are: the low radar frequency that is suboptimal for targets in the Rayleigh scattering regime. The low frequency also experiences more ionospheric propagation effects that degrade measurement quality than more conventional higher frequency radars.

ACKNOWLEDGMENTS

REFERENCES

BPC⁺10. Eli Brookner, Brad Porter, Kaichiang Chang, Yueh-Chi Chang, Dan Zwillinger, Brian Considine, and Tom Sikina. Demonstration of

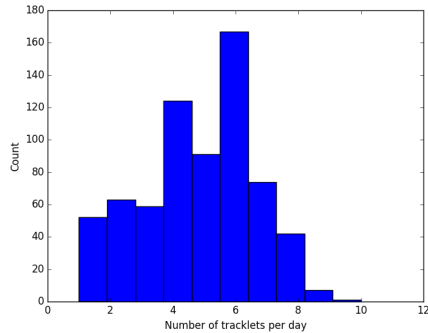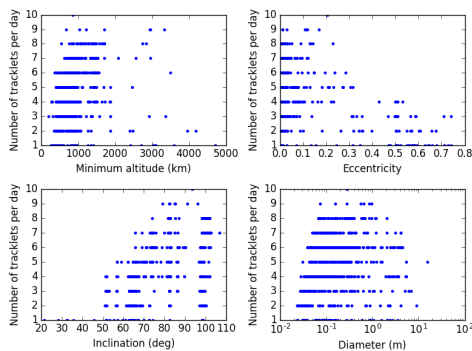accurate prediction of pave paws embedded element gain. In *Phased Array Systems and Technology (ARRAY), 2010 IEEE International Symposium on*, pages 417–422. IEEE, 2010.

BR08. Dieter Bilitza and Bodo W Reinisch. International reference ionosphere 2007: improvements and new parameters. *Advances in Space Research*, 42(4):599–609, 2008.

Bud88. Kenneth George Budden. *The propagation of radio waves: the theory of radio waves of low power in the ionosphere and magnetosphere*. Cambridge University Press, 1988.

EIS14. EISCAT Scientific Association. EISCAT 3D: The next generation international atmosphere and geospace research radar Technical Description. Technical report, 2014.

Eva69. JV Evans. Theory and practice of ionosphere study by thomson scatter radar. *Proceedings of the IEEE*, 57(4):496–530, 1969.

FGW+09. S Flegel, J Gelhaus, C Wiedemann, P Vorsmann, M Oswald, S Stabroth, H Klinkrad, and H Krag. Invited paper: The master-2009 space debris environment model. In *Fifth European Conference on Space Debris*, volume 672, 2009.

KSN+12. Johan Kero, Csilla Szasz, Takuji Nakamura, T Terasawa, H Miyamoto, and K Nishimura. A meteor head echo analysis algorithm for the lower vhf band. In *Annales Geophysicae*, volume 30, page 639. Copernicus GmbH, 2012.

MAA+15. Ian McCrea, Anita Aikio, Lucilla Alfonsi, Evgenia Belova, Stephan Buchert, Mark Clilverd, Norbert Engler, Björn Gustavsson, Craig Heinselman, Johan Kero, et al. The science case for the eiscat_3d radar. *Progress in Earth and Planetary Science*, 2(1):21, 2015.

MLHV02. J Markkanen, M Lehtinen, A Huuskonen, and A Väänänen. Measurements of small-size debris with backscatter of radio waves. *Final report*, 2002.

Tho87. TW Thompson. High-resolution lunar radar map at 70-cm wavelength. *Earth, Moon, and Planets*, 37(1):59–70, 1987.

Val88. Matti Vallinkoski. Statistics of incoherent scatter multiparameter fits. *Journal of atmospheric and terrestrial physics*, 50(9):839–851, 1988.

Vie12. J. Vierinen. Methods and arrangements for detecting weak signals, July 26 2012. WO Patent App. PCT/FI2012/050,041.